Journal of Physics: Conference Series

PAPER • **OPEN ACCESS**

Processing GPR data with 2D Bayesian compressive sensing inverse scattering approaches

To cite this article: P Rocca *et al* 2018 *J. Phys.: Conf. Ser.* **1131** 012006

IOP Conf. Series: Journal of Physics: Conf. Series **1131** (2018) 012006 doi:10.1088/1742-6596/1131/1/012006

Processing GPR data with 2D Bayesian compressive sensing inverse scattering approaches

P Rocca[1], G Gottardi[1], M Bertolli[1], F Robol[1], T Moriyama[2] and T Takenaka[2]

[1] ELEDIA Research Center (ELEDIA@UniTN - University of Trento)
Via Sommarive 9, I-38123 Trento, Italy
[2] ELEDIA Research Center (ELEDIA@UniNAGA - University of Nagasaki)
852-8521, Nagasaki, Japan

E-mail: paolo.rocca@unitn.it

Abstract. In this work, the solution of the subsurface microwave imaging problem is addressed through innovative inverse scattering (*IS*) approaches. Towards this end, wide-band ground penetrating radar (*GPR*) measurements are processed by means of Bayesian Compressive Sensing (*BCS*)-based strategies integrated with frequency-hopping (*FH*) or multi-frequency (*MF*) inversion schemes. Thanks to the additional information provided by the frequency diversity of *GPR* data and the formulation of suitable *sparseness*-regularized methodologies faithful reconstructions are yielded under several operative conditions, as clearly indicated by selected numerical experiments.

1. Introduction

The development of inverse scattering (*IS*) techniques for solving the subsurface microwave imaging problem is nowadays a very attractive field of research given the wide set of civil and military applications. Within this context, ground penetrating radar (*GPR*) is one of the most versatile non-destructive prospecting tool thanks to many favorable features including easy deployment and low cost, making it the perfect candidate for cultural heritage monitoring, civil engineering, forensic investigations, through-the-wall imaging, as well as de-mining [1]-[10]. However, one of the most critical limitations when using *GPR* as probing instrument is the need for high user experience for the correct interpretation of the measured *radargrams*. To overcome such a limitation, several *IS* approaches have been developed in the recent years for the automatic processing of *GPR* data and the generation of easy-to-interpret qualitative and/or quantitative reconstructions of the probed domain [2]-[10]. Among the many proposed strategies, those relying on the exploitation of the intrinsic wide-band nature of *GPR* measurements appeared as effective solutions to the *ill-posedness*/*non-linearity* of the subsurface *IS* problem, where strongly aspect-limited set-ups are typically involved. Several techniques have been proposed to process such multi-chromatic measurements and take advantage of frequency diversity. On the one hand, frequency-hopping (*FH*) schemes [5],[10] process each frequency sample separately and exploit *progressively acquired* information at the low-pass guesses to refine the solution at successive high-frequency inversion stages. On the other hand, multi-frequency (*MF*) methods [6],[8] allow the simultaneous processing of all spectral components in a single-step reconstruction.

Besides the above-mentioned strategies, another effective recipe to counteract the *non-uniqueness* and the *ill-posedness* consists in injecting *a-priori* information about the imaged scenario. This can be done, for instance, by introducing linear models such as those based on the Born approximation in case of weak targets [9]. Otherwise, *sparseness-regularized* solvers such as those based on the Compressive Sensing (*CS*) theory [11]-[14] are able to stabilize the *GPR-IS* problem once a suitable expansion basis is chosen to represent the unknowns with few non-null coefficients.

Following this line of reasoning, this work presents three different strategies based on the integration of Bayesian *CS* (*BCS*) solution approaches with *FH* or *MF* schemes in order to benefit both from the regularization features of sparse priors as well as from multi-chromatic acquisitions.

2. Contrast source formulation of the *GPR-IS* problem

Let us consider the *2D* transverse-magnetic half-space *GPR* prospecting set-up in Fig. 1. A linear interface located at $y = 0$ [m] separates the upper half-space made of air from the lower half-space made of a lossy material with relative permittivity ε_{rB} and conductivity σ_B.

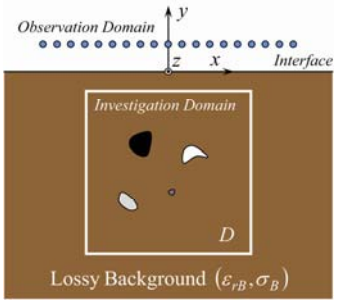

Figure 1. Geometry of the *2D GPR-IS* problem.

A square investigation domain *D*, completely buried below the interface (Fig. 1), is successively imaged by a set of *V* *z*-oriented infinitely-long line sources uniformly spaced at constant height $y = d$ and excited by a wide-band signal covering the frequency range $[f_{\min}, f_{\max}]$. Under the hypothesis that one or multiple unknown objects are embedded inside *D*, the total electric field measured in time-domain by *M* probes co-located with the sources is given by

$$e_{tot}^{v}\left(\mathbf{r}_m^v, t\right) = e_{inc}^{v}\left(\mathbf{r}_m^v, t\right) + e_{scat}^{v}\left(\mathbf{r}_m^v, t\right) + h^{v}\left(\mathbf{r}_m^v, t\right); \quad v = 1,\ldots,V\ ;\ m = 1,\ldots,M \tag{1}$$

where $e_{inc}^{v}\left(\mathbf{r}_m^v, t\right)$ is the incident field, $e_{scat}^{v}\left(\mathbf{r}_m^v, t\right)$ the scattered field, and $h^{v}\left(\mathbf{r}_m^v, t\right)$ an additive Gaussian noise super-imposed to the measured *GPR radargram*. After subtracting the incident field [8], *Q* frequency samples uniformly distributed within the $[f_{\min}, f_{\max}]$ spectrum are extracted from the (noisy) Fourier-transform of the scattered field, i.e.,

$$\hat{E}_{scat}^{v}\left(\mathbf{r}_m^v, f_q\right) = E_{scat}^{v}\left(\mathbf{r}_m^v, f_q\right) + H^{v}\left(\mathbf{r}_m^v, f_q\right); \quad v = 1,\ldots,V\ ;\ m = 1,\ldots,M\ ;\ q = 1,\ldots,Q\,. \tag{2}$$

$H^{v}\left(\mathbf{r}_m^v, f_q\right)$ being the frequency-domain noise. Assuming a contrast source inversion (*CSI*) scheme [15], the goal of the *GPR-IS* problem is to retrieve the *contrast source* defined for $\mathbf{r} \in D$ as follows

$$J^{v}\left(\mathbf{r}, f_q\right) = \tau\left(\mathbf{r}, f_q\right) E_{tot}^{v}\left(\mathbf{r}, f_q\right); \quad v = 1,\ldots,V\ ;\ q = 1,\ldots,Q \tag{3}$$

where $E_{tot}^{v}\left(\mathbf{r}, f_q\right)$ is the frequency-domain total field in *D*, while $\tau\left(\mathbf{r}, f_q\right)$ is the contrast function

$$\tau\left(\mathbf{r}, f_q\right) = \left[\varepsilon_r\left(\mathbf{r}\right) - \varepsilon_{rB}\right] + j\left[\frac{\sigma_B - \sigma\left(\mathbf{r}\right)}{2\pi f_q \varepsilon_0}\right]; \quad q = 1,\ldots,Q \tag{4}$$

mathematically modelling the objects in *D* through their relative permittivity, $\varepsilon_r\left(\mathbf{r}\right)$, and conductivity $\sigma\left(\mathbf{r}\right)$ distributions. To numerically solve the *GPR-IS* problem, *D* is partitioned into *N* square sub-

domains, yielding the following matrix expression where the real ($\Re$) and imaginary ($\Im$) parts of both data and unknowns have been separated [10]

$$\begin{bmatrix} \Re\left(\hat{\mathbf{E}}_{scat}^{v,q}\right) \\ \Im\left(\hat{\mathbf{E}}_{scat}^{v,q}\right) \end{bmatrix} = \begin{bmatrix} \Re\left(\mathbf{G}_{ext}^{v,q}\right) & -\Im\left(\mathbf{G}_{ext}^{v,q}\right) \\ \Im\left(\mathbf{G}_{ext}^{v,q}\right) & \Re\left(\mathbf{G}_{ext}^{v,q}\right) \end{bmatrix} \begin{bmatrix} \Re\left(\mathbf{J}^{v,q}\right) \\ \Im\left(\mathbf{J}^{v,q}\right) \end{bmatrix} + \begin{bmatrix} \Re\left(\mathbf{H}^{v,q}\right) \\ \Im\left(\mathbf{H}^{v,q}\right) \end{bmatrix}; \; v = 1,...,V \; ; \quad q = 1,...,Q \, . \tag{5}$$

In (5) $\hat{\mathbf{E}}_{scat}^{v,q} = \left\{\hat{E}_{scat}^{v}\left(\mathbf{r}_m^v, f_q\right); m = 1,...,M\right\}$ are the scattered field samples under the *v*-th illumination for the *q*-th frequency, $\mathbf{J}^{v,q} = \left\{J^v\left(\mathbf{r}_n, f_q\right); n = 1,...,N\right\}$ contains the unknown contrast sources, $H^{v,q} = \left\{H^v\left(\mathbf{r}_m^v, f_q\right); m = 1,...,M\right\}$ contains the noise samples, while $\mathbf{G}_{ext}^{v,q}$ is the external Green's matrix for the *2D* subsurface problem. Finally, (5) is rewritten in compact form as follows

$$\xi_{scat}^{v,q} = \mathbf{\Phi}_{ext}^{v,q} \boldsymbol{\psi}^{v,q} + \boldsymbol{\rho}^{v,q} \; ; \; v = 1,...,V \; ; \quad q = 1,...,Q \tag{6}$$

where $\xi_{scat}^{v,q}$ is the known data, $\mathbf{\Phi}_{ext}^{v,q}$ is the measurement matrix, $\boldsymbol{\psi}^{v,q}$ is the unknown, and $\boldsymbol{\rho}^{v,q}$ contains the noise samples.

3. BCS solution approaches

3.1. Frequency-hopping (FH) GPR data processing

When considering a *FH* inversion scheme, the solution of (6) is obtained by processing one frequency component of the *GPR* spectrum at a time in a cascaded fashion, starting from the lowest one. At each iteration ($q = 1,...,Q$), the *q*-th unknown vector is estimated as

$$\tilde{\boldsymbol{\psi}}^{v,q} = \arg\left\{\max P\left(\boldsymbol{\psi}^{v,q} \middle| \xi_{scat}^{v,q}\right)\right\}; \; v = 1,...,V \tag{7}$$

where $P\left(\boldsymbol{\psi}^{v,q} \middle| \xi_{scat}^{v,q}\right)$ is the *a-posteriori* probability. Whether the correlation among the several views ($v = 1,...,V$) is enforced, a frequency hopping multi-task *BCS* (*FH-MT-BCS*) solution strategy can adopted, whose solution is given by [16]

$$\tilde{\boldsymbol{\psi}}_{FH-MT-BCS}^{v,q} = \left[diag\left(\tilde{\boldsymbol{\alpha}}^q\right) + \left(\mathbf{\Phi}_{ext}^{v,q}\right)^T \mathbf{\Phi}_{ext}^{v,q} \right]^{-1} \left(\mathbf{\Phi}_{ext}^{v,q}\right)^T \xi_{scat}^{v,q} \; ; \; v = 1,...,V \, . \tag{8}$$

In (8) $.^T$ is the transpose operator, while $\tilde{\boldsymbol{\alpha}}^q$ is the set of $2N$ hyper-parameters shared among the *V* views, determined by solving through a constrained relevance vector machine (*C-RVM*) solver [10]

$$\tilde{\boldsymbol{\alpha}}^q = \arg\left\{ \max_{\boldsymbol{\alpha}^q} \left(-\frac{1}{2} \sum_{v=1}^{V} \left[(2M + 2\beta_1) \log\left(\left(\xi_{scat}^{v,q}\right)^T \left(\mathbf{B}^{v,q}\right)^{-1} \xi_{scat}^{v,q} + 2\beta_2 \right) + \log\left|\mathbf{B}^{v,q}\right| \right] \right) \right\} \tag{9}$$

where $\mathbf{B}^{v,q} = \mathbf{I} + \mathbf{\Phi}_{ext}^{v,q} \left[diag\left(\boldsymbol{\alpha}^q\right) \right]^{-1} \left(\mathbf{\Phi}_{ext}^{v,q}\right)^T$ and (β_1, β_2) are user-defined *MT-BCS* parameters [16] and $\mathbf{I}$ the identity matrix. Given the fact that a pixel basis is exploited to expand the unknown, each hyper-parameter will physically correspond to the real or imaginary part of the contrast source inside the N pixels within D.

On the other hand, if no correlation is enforced among the different illuminations a single-task procedure (*FH-ST-BCS*) can be adopted for solving (7), the contrast sources being estimated as

$$\tilde{\boldsymbol{\psi}}_{FH-ST-BCS}^{v,q} = \frac{1}{\tilde{\sigma}^{v,q}} \left[\frac{\left(\mathbf{\Phi}_{ext}^{v,q}\right)^T \mathbf{\Phi}_{ext}^{v,q}}{\tilde{\sigma}^{v,q}} + diag\left(\tilde{\boldsymbol{\delta}}^{v,q}\right) \right]^{-1} \left(\mathbf{\Phi}_{ext}^{v,q}\right)^T \xi_{scat}^{v,q} \; ; \; v = 1,...,V \, . \tag{10}$$

where $\tilde{\sigma}^{v,q}$ and $\tilde{\boldsymbol{\delta}}^{v,q}$ are the estimated noise variance and the auxiliary *ST-BCS* hyper-parameters (different among the views, $v = 1,...,V$), computed via the *C-RVM* solver as

$$\left(\tilde{\boldsymbol{\delta}}^{v,q},\tilde{\sigma}^{v,q}\right)=\arg\left\{\max_{\left(\boldsymbol{\delta}^{v,q},\boldsymbol{\sigma}^{v,q}\right)}\left(-\frac{1}{2}\left[2M\log 2\pi+\log\left|\mathbf{W}^{v,q}\right|+\left(\boldsymbol{\xi}_{scat}^{v,q}\right)^{T}\left(\mathbf{W}^{v,q}\right)^{-1}\boldsymbol{\xi}_{scat}^{v,q}\right]\right)\right\} \tag{11}$$

where $\mathbf{W}^{v,q}=\sigma^{v,q}\mathbf{I}+\boldsymbol{\Phi}_{ext}^{v,q}\left[diag\left(\boldsymbol{\delta}^{v,q}\right)\right]^{-1}\left(\boldsymbol{\Phi}_{ext}^{v,q}\right)^{T}$. Both the *FH-MT-BCS* and the *FH-ST-BCS* exploit the *acquired* information about the solution at the *q*-th frequency to initialize the *C-RVM* optimization at the $(q+1)$-th step. Towards this end, at each *q*-th step ($q>1$) the set of hyper-parameters to optimize is progressively shrunk to those entries corresponding to cells in *D* falling inside the identified regions-of-interest (i.e., sub-regions of *D* where a potential scatterer has been located at the *q*-th inversion stage) [10]. Finally, the estimated contrast $\tilde{\tau}\left(\mathbf{r}_n,f_q\right)$, $n=1,...,N$, is computed at each frequency from (3) by averaging over the different views ($v=1,...,V$) the ratio between retrieved currents and the corresponding retrieved total fields.

3.2. Multi-frequency (MF) GPR data processing

In order to exploit the frequency diversity of wide-band *GPR* data in a single reconstruction a multi-frequency multi-task *BCS* (*MF-MT-BCS*) approach can be adopted. In this case, the unknown contrast sources are estimated by imposing in (7) that $\boldsymbol{\psi}^{v,q}$ are correlated among the different frequency samples ($q=1,...,Q$) other than among the several views ($v=1,...,V$). Accordingly, the *MF-MT-BCS* solution is computed as

$$\tilde{\boldsymbol{\psi}}_{MF-MT-BCS}^{v,q}=\left[diag\left(\tilde{\boldsymbol{\upsilon}}\right)+\left(\boldsymbol{\Phi}_{ext}^{v,q}\right)^{T}\boldsymbol{\Phi}_{ext}^{v,q}\right]^{-1}\left(\boldsymbol{\Phi}_{ext}^{v,q}\right)^{T}\boldsymbol{\xi}_{scat}^{v,q};\ v=1,...,V;\ q=1,...,Q \tag{12}$$

where the 2*N* shared hyper-parameters $\tilde{\boldsymbol{\upsilon}}$ (among all views and frequencies) are estimated via a *RVM* solver [16] as

$$\tilde{\boldsymbol{\upsilon}}=\arg\left\{\max_{\boldsymbol{\upsilon}}\left(-\frac{1}{2}\sum_{q=1}^{Q}\sum_{v=1}^{V}\left[\left(2M+2\beta_1\right)\log\left(\left(\boldsymbol{\xi}_{scat}^{v,q}\right)^{T}\left(\mathbf{R}^{v,q}\right)^{-1}\boldsymbol{\xi}_{scat}^{v,q}+2\beta_2\right)+\log\left|\mathbf{R}^{v,q}\right|\right]\right)\right\}. \tag{13}$$

where $\mathbf{R}^{v,q}=\mathbf{I}+\boldsymbol{\Phi}_{ext}^{v,q}\left[diag\left(\boldsymbol{\upsilon}\right)\right]^{-1}\left(\boldsymbol{\Phi}_{ext}^{v,q}\right)^{T}$. The contrast function in *D* is then estimated by averaging over the different frequencies ($q=1,...,Q$) and views ($v=1,...,V$) the ratio between retrieved currents and the corresponding retrieved total fields.

4. Numerical comparisons

In order to comparatively assess the proposed *BCS*-based inversion methodologies for solving the *GPR-IS* problem let us consider in the following an investigation domain of side 0.8m buried in a lossy soil with $\varepsilon_{rB}=4$ and $\sigma_B=10^{-3}$ S/m. $V=20$ sources placed at $d=0.1$m over the interface are used to successively probe *D* with wide-band pulses in the $\left[f_{\min},f_{\max}\right]=\left[200,600\right]$MHz band. $M=19$ probes are used each time to collect the *GPR* time-domain data, which is successively transformed to the frequency-domain where $Q=9$ spectral components are extracted for the inversion. The *FDTD*-based solver *GPRMax2D* [8] has been exploited to synthesize the time-domain radargrams, while a custom FORTRAN implementation of the *2D* Method of Moments (*MoM*) has been adopted for implementing the external Green's matrix and solving the inverse problem.

Figure 2 shows the real part of the contrast retrieved by the *MF-MT-BCS* [Fig. 2(*b*)], the *FH-MT-BCS* [Fig. 2(*c*)], and the *FH-ST-BCS* [Fig. 2(*d*)] when considering the "*Three-Pixel*" scatterer in Fig. 2(*a*) ($\varepsilon_r^{obj}=5.5$ and $\sigma^{obj}=10^{-4}$ S/m) and a signal-to-noise-ratio (on time-domain total field) equal to $SNR=40$ dB. As it can be seen, faithful reconstructions are yielded by the two *MT-BCS* approaches, which are both able to correctly detect the presence of the scatterer [Figs. 2(*b*)-2(*c*)], while the *FH-ST-BCS* solution is less accurate with a lot of undesired artifacts in the background region [Fig. 2(*d*)].

Moreover, it should be pointed out that imposing the correlation among different frequency components of the scattered data allows a significant enhancement of the *MF-MT-BCS* solution quality [Fig. 2(*b*)] with respect to the *FH-MT-BCS* one [Fig. 2(*c*)].

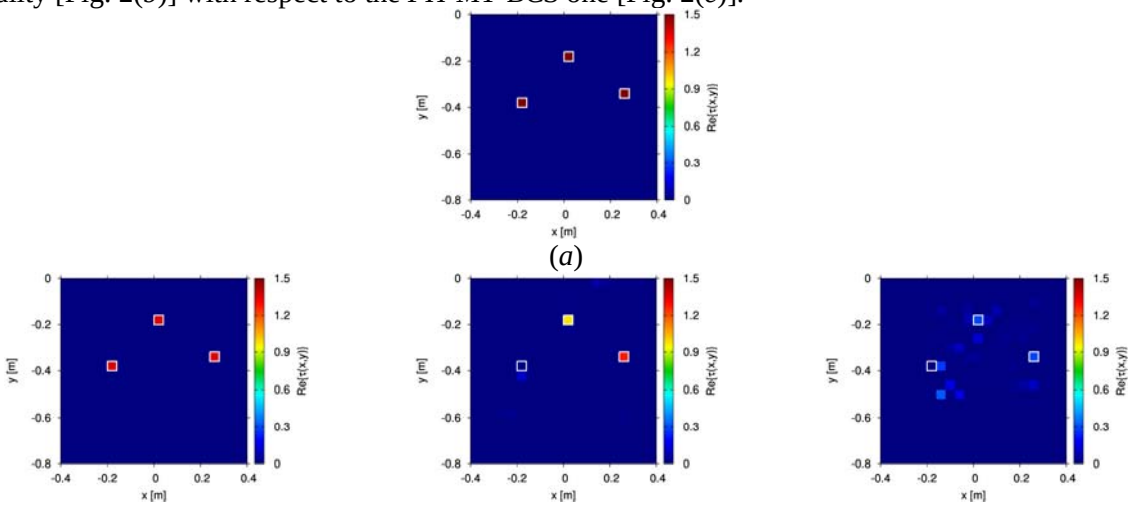

(*a*)

(*b*) (*c*) (*d*)

Figure 2. *Numerical Comparison* (*Three-Pixels Scatterer*, $\varepsilon_r^{obj} = 5.5$, $\sigma^{obj} = 10^{-4}$ S/m, $SNR = 40$ dB) – Real part of (*a*) the actual contrast profile and of the retrieved solutions by the (*b*) *MF-MT-BCS*, (*c*) *FH-MT-BCS*, and (*d*) *FH-ST-BCS* methods.

Similar conclusions can be drawn by looking at the imaginary part of the retrieved contrasts in Fig. 3, where the superiority of the multi-frequency inversion strategy is even more evident over the two frequency-hopping alternatives [Fig. 3(*b*) vs. Figs. 3(*c*)-3(*d*)].

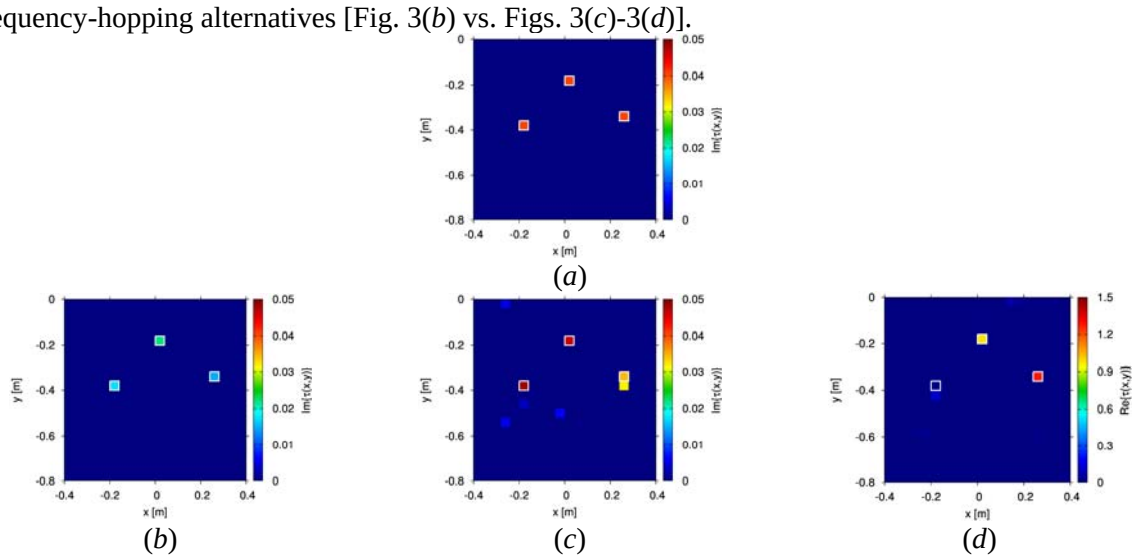

(*a*)

(*b*) (*c*) (*d*)

Figure 3. *Numerical Comparison* (*Three-Pixels Scatterer*, $\varepsilon_r^{obj} = 5.5$, $\sigma^{obj} = 10^{-4}$ S/m, $SNR = 40$ dB) – Imaginary part of (*a*) the actual contrast profile and of the retrieved solutions by the (*b*) *MF-MT-BCS*, (*c*) *FH-MT-BCS*, and (*d*) *FH-ST-BCS* methods.

To further investigate the performance of the three *BCS GPR-IS* methods, let us consider in the following the retrieval of the "*Two-Bars*" profile in Fig. 5(*a*) ($\varepsilon_r^{obj} = 7.0$, $\sigma^{obj} = 10^{-3}$ S/m). A significant boost in terms of reconstruction accuracy is achieved by the *MF-MT-BCS* [Fig. 5(*b*)], providing a better estimation of the contrast value with respect to the *FH-MT-BCS* [Fig. 5(*c*)] and a remarkably improved solution when compared to the *FH-ST-BCS* [Fig. 5(*d*)].

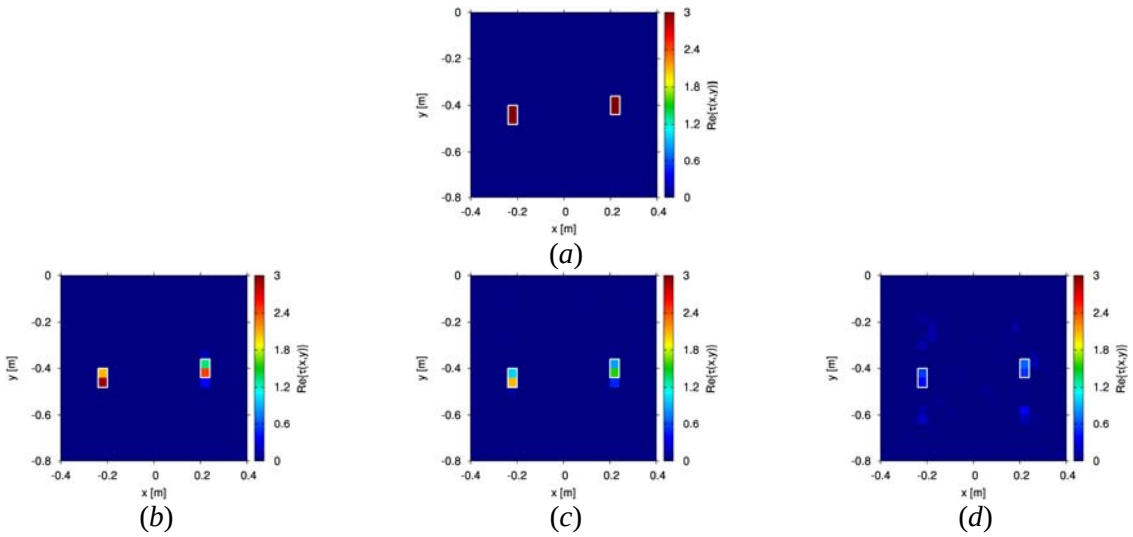

Figure 4. *Numerical Comparison* (*Two-Bars Scatterer*, $\varepsilon_r^{obj} = 7.0$, $\sigma^{obj} = 10^{-3}$ S/m, $SNR = 40$ dB) – Real part of (*a*) the actual contrast profile and of the retrieved solutions by the (*b*) *MF-MT-BCS*, (*c*) *FH-MT-BCS*, and (*d*) *FH-ST-BCS* methods.

Finally, the total reconstruction error, defined as in [10] is reported in Fig. 5 as a function of the actual relative permittivity of the same scatterer of Fig. 4(*a*). As it can be noticed, the *FH-ST-BCS* solutions are always significantly worse than those of the two *MT* approaches since no correlation among the different views is exploited. Moreover, this result further verifies that the *MF-MT-BCS* is the more robust strategy, leading to lower reconstruction errors in presence of both weak and strong targets (Fig. 5).

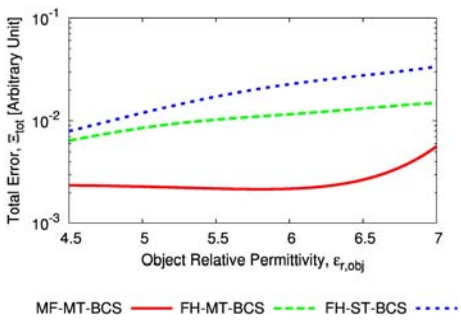

Figure 5. *Numerical Comparison* (*Two-Bars Scatterer*, $\sigma^{obj} = 10^{-3}$ S/m, $SNR = 40$ dB) – Total reconstruction error versus the relative permittivity of the object.

5. Conclusions

The processing of wide-band *GPR* data through *BCS*-based inverse scattering techniques has been addressed in this work. The proposed approaches allow to exploit the intrinsic frequency-diversity of *GPR* measurements through frequency-hopping (*FH*) or multi-frequency (*MF*) solution strategies, as well as benefit from the sparseness-driven regularization features of *BCS*. From a methodological point of view, the main novelties are the development of a *C-RVM* solver to exploit progressively acquired information from low-pass to high-pass solutions in *FH* schemes and the formulation of the *GPR-IS* problem within a *MF-CSI* framework enabling the exploitation of the existing correlation among several frequencies and views. Selected numerical results have been shown in order to comparatively assess the performances of three *BCS* implementations. The reported results indicate that (*i*) correlating the several views through multi-task (*MT*) approaches allow to significantly reduce the reconstruction error with respect to single-task (*ST*) strategies and (*ii*) jointly processing the frequency samples of the *GPR* spectrum through the *MF-MT-BCS* method provides more robust

reconstructions under several operative conditions. Future works will be devoted at assessing the three techniques on real experimental data, as well as to extend them to deal with a *3D* formulation of the subsurface imaging problem.

Acknowledgment
This work has been partially supported by the Italian Ministry of Foreign Affairs and International Cooperation, Directorate General for Cultural and Economic Promotion and Innovation within the SNATCH Project (2017-2019).

References

[1] Peters L, Daniels J and Young J D 1994 Ground penetrating radar as a subsurface environmental sensing tool *IEEE Proc.* **82** 1802–1822
[2] Lesselier D and Habashy T 2000 Special issue on electromagnetic imaging and inversion on the Earth's subsurface *Inverse Probl.* **16**
[3] Li M, Abubakar A and Habashy TM 2010 Application of a two-and-half dimensional model-based algorithm to crosswell electromagnetic data inversion *Inverse Probl.* **26** 1-17
[4] Abubakar A, Habashy TM, Li M and Liu J 2009 Inversion algorithm for large-scale geophysical electromagnetic measurements *Inverse Probl.* **25** 1-30
[5] Salucci M, Oliveri G and Massa A 2015 GPR prospecting through an inverse scattering frequency-hopping multifocusing approach *IEEE Trans. Geosci. Remote. Sens.* **53** 6573-6592
[6] Salucci M, Poli L and Massa A 2017 Advanced multi-frequency GPR data processing for non linear deterministic imaging *Signal Processing* **132** 306-318
[7] Krueger KR, McClellan JH, Scott WR 2015 Efficient algorithm design for GPR imaging of landmines *IEEE Trans. Geosci. Remote Sens.* **53** 4010-4021
[8] Salucci M, Poli L, Anselmi N and Massa A 2017 Multifrequency particle swarm optimization for enhanced multiresolution GPR microwave imaging *IEEE Trans. Geosci. Remote Sens.* **55** 1305-1317
[9] Salucci M, Oliveri G, Randazzo A, Pastorino M and Massa A 2014 Electromagnetic subsurface prospecting by a multifocusing inexact Newton method within the second-order Born approximation *J. Opt. Soc. Am. A* **31** 1167-1179
[10] Salucci M, Gelmini A, Poli L, Oliveri G and Massa A 2018 Progressive compressive sensing for exploiting frequency-diversity in GPR imaging *Journal of Electromagnetic Waves and Applications* ***32*** *1164-1193*
[11] Oliveri G, Salucci M, Anselmi N and Massa A 2017 Compressive sensing as applied to inverse problems for imaging: theory, applications, current trends, and open challenges *IEEE Antennas Propag. Mag*. **59** 34-46
[12] Sun Y, Qu L, Zhang S and Yin Y 2016 MT-BCS-based two-dimensional diffraction tomographic GPR imaging algorithm with multiview-multistatic configuration *IEEE Geosci. Remote Sens. Lett.* **13** 831-835
[13] Suksmono AB, Bharata E, Lestari AA, Yarovoy AG and Lightart LP 2010 Compressive stepped-frequency continuous-wave ground-penetrating radar *IEEE Geosci. Remote Sens. Lett.* **7** 665-669
[14] Anselmi N, Oliveri G, Hannan M A, Salucci M and Massa A 2017 Color compressive sensing imaging of arbitrary-shaped scatterers *IEEE Trans. Microw. Theory Techn.* **65** 1986-1999
[15] Li M, Semerci O and Abubakar A 2013 A contrast source inversion method in the wavelet domain *Inverse Probl.* **29** 025015
[16] Ji S, Dunson D and Carin L 2009 Multitask compressive sensing *IEEE Trans. Signal Process.* **57** 92-106